

Topological Node-Line Semimetal in Three Dimensional Graphene Networks

Hongming Weng,^{1,2,*} Yunye Liang,³ Qiunan Xu,¹ Rui Yu,⁴ Zhong Fang,^{1,2} Xi Dai,^{1,2} and Yoshiyuki Kawazoe^{3,5}

¹*Beijing National Laboratory for Condensed Matter Physics, and Institute of Physics, Chinese Academy of Sciences, Beijing 100190, China*

²*Collaborative Innovation Center of Quantum Matter, Beijing, China*

³*New Industry Creation Hatchery Center, Tohoku University, Sendai, 980-8579, Japan*

⁴*International Center for Materials Nanoarchitectonics (WPI-MANA), National Institute for Materials Science, Tsukuba 305-0044, Japan*

⁵*Thermophysics Institute, Siberian Branch, Russian Academy of Sciences, Russia*

(Dated: May 22, 2015)

Abstract

Graphene, a two dimensional (2D) carbon sheet, acquires many of its amazing properties from the Dirac point nature of its electronic structures with negligible spin-orbit coupling. Extending to 3D space, graphene networks with negative curvature, called Mackay-Terrones crystals (MTC), have been proposed and experimentally explored, yet their topological properties remain to be discovered. Based on the first-principle calculations, we report an all-carbon MTC with topologically non-trivial electronic states by exhibiting node-lines in bulk. When the node-lines are projected on to surfaces to form circles, “drumhead”-like flat surface bands nestled inside of the circles are formed. The bulk node-line can evolve into 3D Dirac point in the absence of inversion symmetry, which has shown its plausible existence in recent experiments.

I. INTRODUCTION

Carbon is one of the most fascinating elements in nature, which can form many different crystal structures with diverse electronic properties, such as C_{60} ,¹ nanotube,² graphene,³ graphite, and diamond. Among them, graphene is one of the most amazing materials, which supports Dirac point in its low energy electronic structure, described as $H = v\vec{k} \cdot \vec{\sigma}$, where v is velocity, $\vec{k} = (k_x, k_y)$ is momentum and $\vec{\sigma}$ is Pauli matrix. This novel electronic state leads to many interesting phenomena, such as the unconventional quantum Hall effect, large magnetoresistance, and unusual optical properties, which make graphene potentially useful.⁴ The presence of 2D Dirac cone is fragile, and two conditions are required to protect it: (1) the absence of spin-orbit coupling (SOC), and (2) the presence of inversion symmetry. The first condition is naturally satisfied in graphene, because its SOC strength is negligible ($\sim 10^{-3}$ meV).⁵ If SOC in graphene is taken into account, it will open up a gap at Fermi level and lead to quantum spin Hall insulator (i.e., 2D topological insulator).⁶ The second requirement is, however, very strong, and it is satisfied only in the presence of A-B sublattice symmetry, which can be easily broken, leading to a normal insulating state, similar to that in BN nanosheet.

As proposed by A. L. Mackay and H. Terrones,⁷ graphene can be extended to three-dimensional (3D) space to form 3D networks by placing graphitic tiles consisting of 4- to 8-membered rings onto the Schwarz minimal surface. Hereafter, we call such 3D all carbon allotrope Mackay-Terrones crystal (MTC). Schwarz minimal surface is a 3D periodic minimal surface with its mean curvature $H = (k_1 + k_2)/2$ being zero and Gaussian curvature ($K = k_1 k_2$) being negative everywhere on it. Here k_1 and k_2 are the principal curvatures. There are various Schwarz minimal surfaces, such as primitive (P), diamond (D) and gyroid (G) surface. One type of MTC based on P-surface is shown in Fig. 1. Different from C_{60} -like fullerene, which has positive Gaussian curvature, MTC has negative Gaussian curvature and is periodically connected. Such 3D network of sp^2 -bonded carbon has unique properties, such as high surface-to-volume ratio and remarkable porosity, which stimulate extensive studies.^{8,9} Theoretically, MTC has been proved to be dynamically stable and require less formation energy than C_{60} .^{10,11} Experimentally, saddle-like nano-carbon sheet, the main component of MTC, has been successfully synthesized.¹² Similar negatively curved sp^2 networks has been observed in spongy carbon¹³ and negative replica of zeolite.¹⁴ Recently, high-quality

3D nanoporous graphene fabricated by using nanoporous Ni as template shows very similar MTC structure,^{15,16} making synthesizing of it very promising. On the other hand, the topological properties of the band structure for these all-carbon MTC remain unexplored and will be the main subject of this paper. We will show that such all-carbon MTC can host non-trivial electronic states, including topological node-lines and 3D Dirac points, which are distinct from its 2D counter material graphene.

II. RESULTS

We concentrate on the MTC formed with Schwarz minimal P-surface. As shown in Fig. 1, a stable structure with simple cubic lattice in $Pm\bar{3}m$ space group, and 176 atoms per unit cell has been obtained by Tagami *et al.* in Ref. 17 and labeled as 6-1-1-p. We have employed the software package OpenMX¹⁸ for the first-principles calculation. It is based on norm-conserving pseudopotential and pseudo-atomic localized basis functions, which is highly efficient for the MTC with more than a hundred atoms. The choice of pseudopotentials, pseudo atomic orbital basis sets C6.0-s2p2d1 and the sampling of Brillouin zone with $10 \times 10 \times 10$ -grid have been carefully checked. After full structural relaxation, we get the lattice constant $a=14.48 \text{ \AA}$, and the diameters of the pipes or pores are around 9.876 \AA and 5.629 \AA , respectively, which are in good agreement with their results.¹⁷ The electronic band structure of this crystal, calculated based on the local density approximation (LDA), is shown in Fig. 1(d). We find that this crystal is a semimetal with band crossings around the Fermi level, similar to the massless Dirac cone in graphene, but they are in fact very different – the key issue of this paper.

A. Band structure

Detailed analysis of the band structure reveals that: (1) The occupied and unoccupied low energy bands are triply-degenerate at Γ , and have T_{1g} and T_{2u} symmetry, respectively. The formers are even while the laterers are odd under spacial inversion symmetry. Moving from Γ to R point, their degeneracy recover again. However, their energy ordering exchanges, leading to the so called band inversion, which is one of the key ingredients for the topological insulators.^{19,20} Due to the band inversion, the band crossings happen along both $X - R$ and

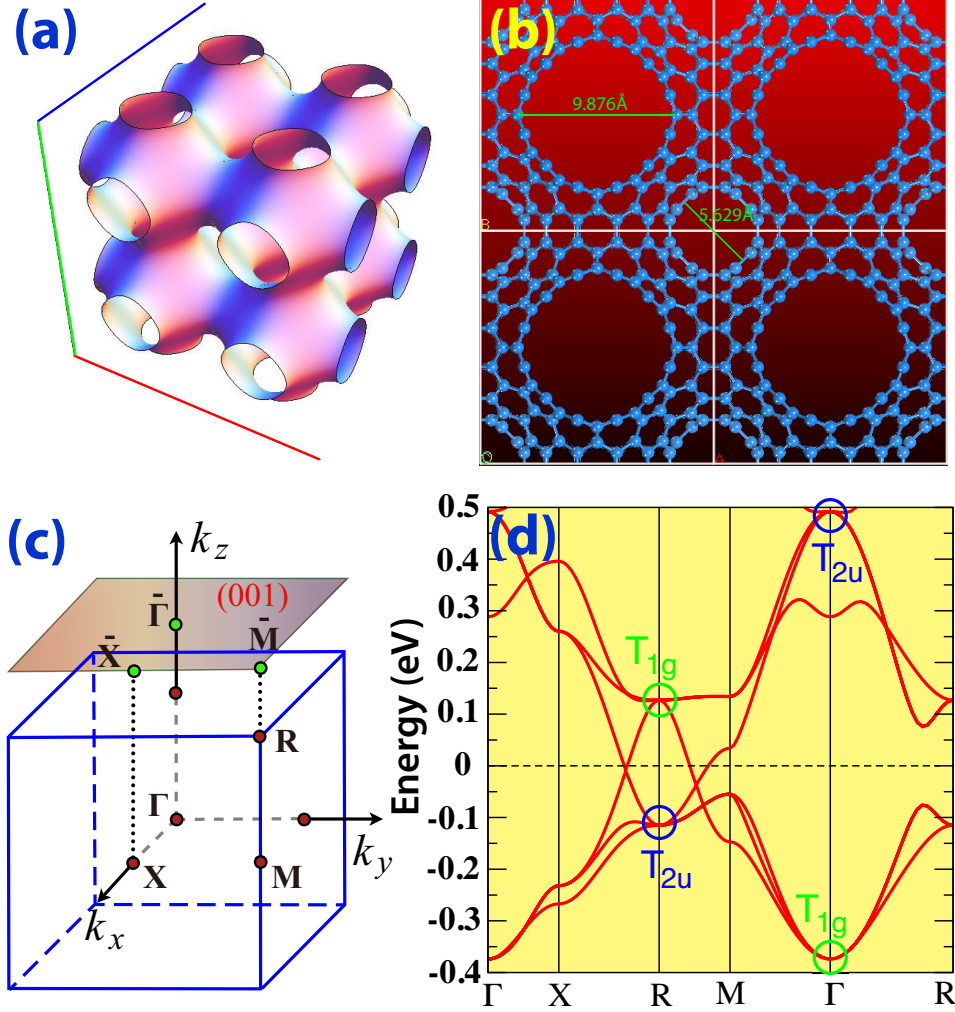


FIG. 1: (Color online) (a) The Schwarz minimal P-surface in $2 \times 2 \times 2$ supercell. (b) The top view of 6-1-1-p MTC in 2×2 supercell. (c) Bulk and (001)-surface Brillouin zone, as well as the high symmetrical k-points. (d) Band structure from the first-principles calculation. The two triply degenerated eigenstates at Γ and R with T_{1g} and T_{2u} symmetrical representation are marked. The band inversion between them can be easily seen.

$R - M$ paths as seen from Fig. 1(d). (2) Including SOC in the calculation, a gap will open up around the band crossings, leading to a 3D strong topological insulator with Z_2 index of $(1;111)^{21}$ by treating the lower half of the anti-crossing bands as occupied. However, similar to graphene, the SOC splitting is small (around 0.13 meV or 1.5 K), and can be neglected in cases with temperature higher than 1.5 K.

The low energy bands near the Fermi level are formed by the overlapping of the molecular orbitals with T_{1g} and T_{2u} symmetry. Since each isolated carbon cluster in the MTC has

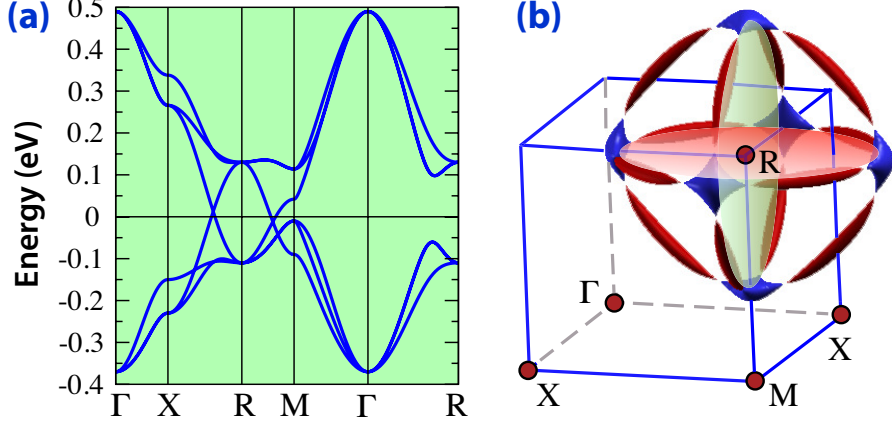


FIG. 2: (Color online) (a) Band structure from effective tight-binding model calculation, which reproduces all the features of Fig. 1(d). (b) Fermi surface consists of three lotus root like rings. These rings are centering R point and parallel to the $k_x=\frac{\pi}{a}$, $k_y=\frac{\pi}{a}$ and $k_z=\frac{\pi}{a}$ plane, respectively. They are formed by the electron pockets (blue) and hole pockets (red) connected by nodal points at Fermi energy.

approximately spherical symmetry, these molecular orbitals can be viewed as the “atomic orbitals” with g and f -wave symmetry, which are further splitted under the cubic crystal field. Therefore, the T_{1g} sector consists of $g_{xy}(x^2-y^2)$, $g_{yz}(y^2-z^2)$ and $g_{zx}(z^2-x^2)$ orbitals, while the T_{2u} sector contains $f_x(y^2-z^2)$, $f_y(z^2-x^2)$, and $f_z(x^2-y^2)$ orbitals. Thus, these six hypothetical atomic orbitals are used as basis set to reproduce the low energy physics of this system. A Slater-Koster tight-binding (TB) Hamiltonian has been established and the on-site energy levels, as well as hopping parameters, can be obtained by fitting the band structure from the first-principles calculations. (see Appendix for details) The triply degenerated T_{1g} and T_{2u} bands at Γ have eigen energies of $E_g + 4V_{gpp} + 2V_{gpd}$ and $E_f - 4V_{ffd}$, respectively. Those at R are $E_g - 4V_{gpp} - 2V_{gpd}$ and $E_f + 4V_{ffd}$ due to the nearest-neighbor hopping. Here, E_g and E_f are on-site energies for g and f orbitals. V_{gpp} and V_{gpd} are the hopping parameters among g orbitals. V_{ffp} and V_{ffd} are those for f -orbitals. From these analysis, we learn that the band inversion or the switching of g (T_{1g}) and f (T_{2u}) orbitals between Γ and R points is due to the strong energy dispersion (or the large hopping parameters). As shown in Fig. 2, this TB model can reproduce all the features of bands, including band topology, with the fitted Slater-Koster parameters (in unit eV) $E_g=-0.12$, $E_f=0.19$, $V_{ffp}=0.019$, $V_{ffd}=-0.075$, $V_{fpp}=0.05$, $V_{fgd}=0.0$, $V_{gpp}=-0.035$, $V_{gpd}=-0.055$. The mean square error is minimized

to 0.0016 eV² with sampling k-points along the high-symmetrical path shown in Fig. 1(d). Artificially reducing the hopping parameters (such as expanding the lattice parameter) by 50% will eliminate the band inversion, with T_{1g} states lower than the T_{2u} states at R point. This calculation also suggests that the strength of band inversion in the system is strong.

B. Topological Node-Lines and 3D Dirac Points

Interestingly, the band crossings in MTC lead to node-lines rather than node points. In other words, the band crossings exist along certain closed loops in the 3D momentum space, and generate three circular-like node-lines around the *R* point, as shown in Fig. 2. These node-lines are protected by two factors, one is the coexistence of time reversal (T) and spacial inversion (P) symmetry and the other factor is that the SOC is negligible.

With the coexistence of P and T symmetries, there exists a certain gauge choice under which the spineless Hamiltonian is completely real valued. (See Appendix for details) Now we will show that for this system, if there is an energy level-crossing of two bands at a momentum \mathbf{k}_0 , a stable node-line will unavoidably appear. Around the crossing point, the two-level 2×2 Hamiltonian can be written in the following general form:

$$\mathcal{H} = d_0(\vec{k}) + d_x(\vec{k}) \cdot \sigma_x + d_y(\vec{k}) \cdot \sigma_y + d_z(\vec{k}) \cdot \sigma_z, \quad (1)$$

where the Pauli matrices $\sigma_i (i=x, y, z)$ denote the two-band space. Without loss of generality, $d_i(\vec{k}) (i=0, x, y, z)$ are all real function of \vec{k} . The eigen energy of \mathcal{H} being

$$E(\vec{k}) = \pm \sqrt{d_x^2(\vec{k}) + d_y^2(\vec{k}) + d_z^2(\vec{k})} + d_0(\vec{k}), \quad (2)$$

and the energy degeneracy can be obtained when the three conditions $d_i(\vec{k})=0 (i=x, y, z)$ are satisfied with three parameters $\vec{k}(k_x, k_y, k_z)$ in the 3D momentum space. As mentioned above, the Hamiltonian can be chosen to be real valued leading to $d_y = 0$. The rest $d_0(\vec{k})$, $d_x(\vec{k})$ and $d_z(\vec{k})$ can be expanded around k_0 and the location of the crossing points can be determined by $d_x(\vec{k}_0) \approx \delta_x + \vec{v}_x(\vec{k} - k_0) = 0$ and $d_z(\vec{k}_0) \approx \delta_z + \vec{v}_z(\vec{k} - k_0) = 0$, where $\vec{v}_i = \vec{\nabla}_{\vec{k}} d_i(\vec{k})$ and δ_i denote the small perturbative terms with both T and P symmetries. In the generic case, the above two equations give a line in the vicinity of k_0 with its direction determined by $\vec{v}_x \times \vec{v}_z$. Therefore, the generic solution of the band crossing point in 3D k-space is a closed loop. Any external perturbations that keep T, P and translational symmetry can only shift or distort but not eliminate the nodal loops.

The topologically stable node-line in MTC is only protected by P and T and no other symmetry is required. The additional mirror symmetry in the present system only forces the node-lines to stay in k_z (or $k_x, k_y = \frac{\pi}{a}$) plane. The cubic symmetry leads to three in-plane node-lines, as what have been found from our calculations in Fig. 2. The node-lines are not necessarily to be flat in energy, and they can have energy dispersion in the k space determined by $d_0(\mathbf{k})$ term (which breaks the particle-hole symmetry). Different from other proposals for the topological node-lines,²² the appearance of node-lines in MTC is very stable and does not require fine tuning of any parameters. This mechanism to generate topological node-lines in three dimensional materials only requires T, P symmetry and weak enough SOC, which can be easily applied to a large class of materials consisting of mainly the light elements.

It is now clear that this 3D MTC is different with graphene in the sense that it is a semimetal with node-lines in the 3D momentum space with the presence of both T and P symmetries. The thing becomes even more interesting if P symmetry is further broken. In such a case, from above discussions, we will in general expect three conditions $d_i(\mathbf{k}) = 0$ with three parameters for the band crossing points, leading to isolated points in the 3D k-space. This is nothing but the 3D Dirac metals discussed recently.²³⁻²⁸ On the other hand, comparing with other proposals for Dirac semimetals, the 3D Dirac point here is topologically stable and does not require the protection from any crystalline symmetry. Similar with the situation in graphene, finite SOC will open a gap at the Dirac point and makes the system a topological insulator. In fact, although our calculated structure has inversion symmetry, most of known real samples of MTC^{15,16} have strong defects and orientation disorder, which should break inversion symmetry. The plausible existence of these stable 3D Dirac points has been indicated by the density of states¹⁵ and heat capacity measurements.²⁹ If T symmetry is further broken in the system, we will expect Weyl semimetal states, which has been extensively studied but not realized yet experimentally.³⁰⁻³³

C. Fermi surface and surface flat band

The two crossing bands within the $k_z = \frac{\pi}{a}$ plane obtained by TB Hamiltonian are plotted in Fig. 3. In general the crossing of bands do not happen at the same energy. They have energy dispersion around 25 meV. The alternative electron and hole pockets are formed

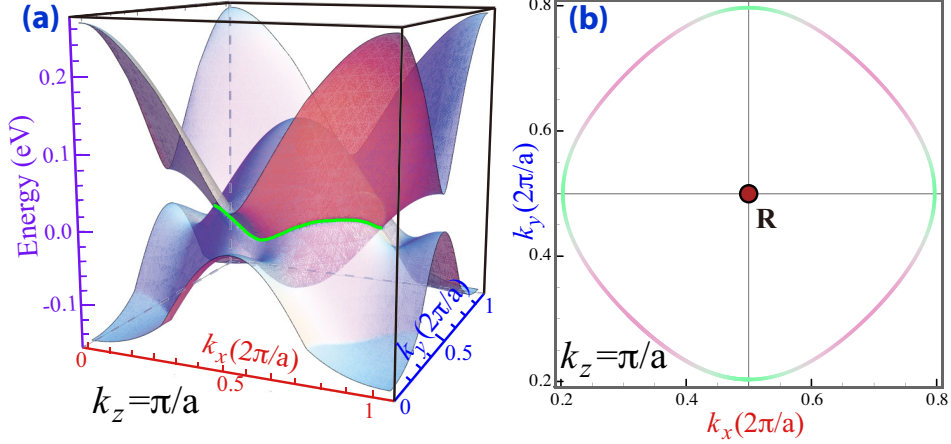


FIG. 3: (Color online) (a) Band crossings of the two bands near Fermi level form node-line (in Green) in $k_z = \frac{\pi}{a}$ plane. (b) The crossing happens at different eigen energy as indicated by different color, the greener the lower in energy.

when the band crossing is lower or higher than the Fermi level and this results in lotus-root like Fermi surface instead of dispersionless line.

This topologically stable node-line semimetal state can have nontrivial surface states.^{22,34-37} For the (001)-surface, the three node-line rings are projected to be a ring and two orthogonal diameter segments inside of it as shown in Fig. 4(a). The (001)-surface state is calculated based on the six-band TB model using both Green’s function method and slab-model method.³⁸ There is a nearly flat surface band nestled inside of the projected node-line ring with its band width being about 40 meV due to the particle-hole asymmetry. The peak-like surface density of states contributed by this nearly flat band is clearly shown in Fig. 4(b), which is proposed to be an important route to high temperature surface superconductivity.^{39,40} The layer-resolved weight of wave function for the surface flat band is shown in Fig. 4(c). It penetrates just three layers into bulk with most of the weight on the surface layer. The surface localization of these flat bands is well resolved for those separated from bulk bands. The nestled flat surface states have small dispersion and their eigen energy distribution in surface BZ is shown in Fig. 4(d), which looks like some vibrational mode of “drumhead”. Such “drumhead”-like states are readily to be detected by angle-resolved photoelectron spectroscopy or scanning tunnel microscope.

The topological node-line state, as well as its surface flat band, can be understood by studying an effective 2×2 toy model Hamiltonian. Taking $d_x = k_z$, $d_y = 0$ and $d_z = M - B(k_x^2 +$

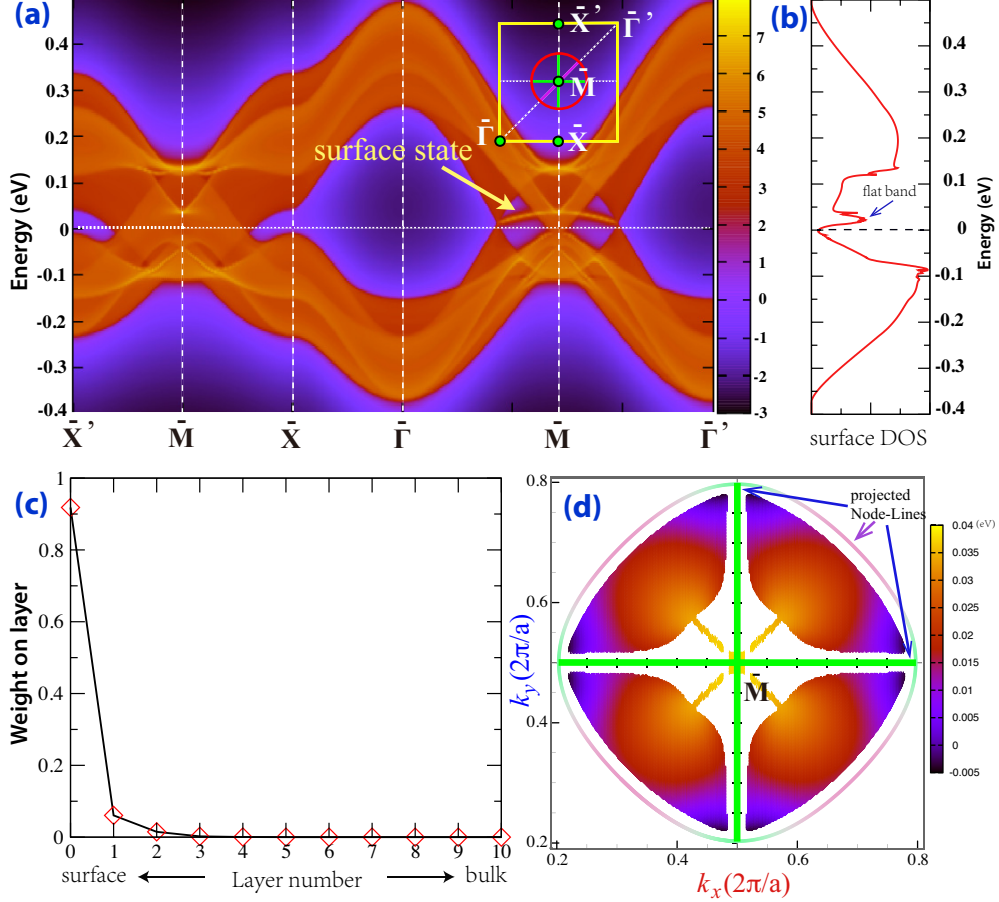


FIG. 4: (Color online) The (001)-surface state. (a) The nearly flat surface band is nestled between two solid Dirac cones, which are the projection of one of the node-line circles as indicated in the inset (red circle). The other two node-line rings are projected as two orthogonal diameters (green line). (b) The surface density of state. (c) The wave function of surface state pointed by the arrow decay rapidly into bulk. (d) The eigen energy distribution of surface flat band nestled inside of projected node-line circle, which looks like a vibration model of “drumhead”. The mixing of surface and bulk state leads to discontinuous in this plot.

$k_y^2 + k_z^2$), the Hamiltonian gives a node-line determined by $k_x^2 + k_y^2 = \frac{M}{B}$ in the plane $k_z=0$. Obviously $\frac{M}{B} > 0$ is required. The topology of this effective continuum bulk hamiltonian has been analyzed⁴¹ (See Appendix for details) and found to have topologically protected (001) surface states with dispersionless zero eigen energy inside of the projected node-line circle given by $\bar{k}_x^2 + \bar{k}_y^2 = \frac{M}{B}$. Here (\bar{k}_x, \bar{k}_y) denotes the k-point in (001) surface Brillouin zone. As mentioned above, $d_0(\vec{k})$ determines the energy dispersion of the node-line, as well

as the surface flat band, though the detailed dispersion of surface states are also influenced by the surface potential in practice.³⁸

III. DISCUSSION

We find that 6-1-1-p is not the only MTC having such novel node-line semimetal state. The MTC with the structure labeled as 6-1-2-p¹⁷ also has such nontrivial topological state. (as shown Appendix) The differences are: (1) The band inversion happens at M point and the Z_2 index is (1;000) when even weaker SOC splitting (about 0.03 meV compared with 0.136 meV in 6-1-1-p) is considered. (2) The low energy physics around Fermi level can be described by six atomic like molecular orbitals also, but they are T_{1u} (p_x , p_y and p_z) and T_{2g} (d_{xy} , d_{yz} and d_{xz}). The similar tight-binding model on simple cubic lattice can also reproduce all of its electronic structure. (3) There are also three mutually perpendicular line-node circles centering M point instead of R point. The similar surface state with nearly flat band can also be obtained. Therefore, it is most plausible that there are more 3D MTCs which can host such node-line semimetal state. Similar node-lines have also been found in optimally tuned photonic crystal composed of gyroid,⁴² the Schwarz minimal G-surface. Other proposed carbon system include Bernal graphite^{43,44} and hyper-honeycomb lattice.⁴⁵ A carbon gyroid⁴⁶ is found to be metal with Dirac cone in conduction bands higher away from Fermi level. Node-line is also proposed in Dirac or Weyl superconductors.⁴⁷

IV. CONCLUSION

In summary, based on the first-principles calculations, we have predicted that a family of all-carbon 3D allotrope, Mackay-Terrones crystals, can have nontrivial topological node-line semimetal state, which is protected by both time-reversal symmetry and inversion symmetry after band inversion. When such bulk node-line is projected onto surface to form a circle, there is flat bands nestled inside of it. Such “drumhead”-like state is an ideal playground for many interaction induced nontrivial states, such as superconductivity and fractional topological insulator states. Further, if the inversion symmetry is broken, the node-lines will evolve into stable 3D Dirac points. Two examples of such MTC with stable structure have been discussed. These predications can most probably be directly observed in further

experiments.

V. ACKNOWLEDGMENTS

H.M.W., Z.F. and X.D. acknowledge the supports from National Natural Science Foundation of China, the 973 program of China (No. 2011CBA00108 and 2013CB921700) and the "Strategic Priority Research Program (B)" of the Chinese Academy of Sciences (No. XDB07020100). H.M.W. thanks the hospitality during his stay in Tohoku University and part of this work has been done there. Y.K. acknowledges to the Russian Megagrant project grant No. 14.B25.31.0030. Both Y.L. and Y.K. are supported by JST, CREST, "A mathematical challenge to a new phase of material sciences" (2008-2013).

Note: During the reviewing of this work, we noticed that a similar work from Y. Chen *et al.*⁴⁸, in which the Node-line, the nestled nearly flat surface bands and the stable 3D Dirac nodes due to inversion symmetry breaking proposed in this manuscript are also obtained for another carbon system.

* Electronic address: hmweng@iphy.ac.cn

¹ H W Kroto, J R Heath, S C O'Brien, R F Curl, and R E Smalley. C60: Buckminsterfullerene. *Nature*, 318(6042):162–163, November 1985.

² Sumio Iijima. Helical microtubules of graphitic carbon. *Nature*, 354(6348):56–58, November 1991.

³ K. S. Novoselov, A. K. Geim, S. V. Morozov, D. Jiang, Y. Zhang, S. V. Dubonos, I. V. Grigorieva, and A. A. Firsov. Electric field effect in atomically thin carbon films. *Science*, 306(5696):666–669, 2004.

⁴ A K Geim and K S Novoselov. The rise of graphene. *Nature Materials*, 6(3):183–191, March 2007.

⁵ Yugui Yao, Fei Ye, Xiao-Liang Qi, Shou-Cheng Zhang, and Zhong Fang. Spin-orbit gap of graphene: First-principles calculations. *Phys. Rev. B*, 75:041401, Jan 2007.

⁶ C. L. Kane and E. J. Mele. Quantum spin hall effect in graphene. *Phys. Rev. Lett.*, 95:226801, Nov 2005.

- ⁷ A L Mackay and Terrones H. Diamond from graphite. *Nature*, 352(6338):762, August 1991.
- ⁸ Rodney S. Ruoff. Personal perspectives on graphene: New graphene-related materials on the horizon. *MRS Bulletin*, 37:1314–1318, 12 2012.
- ⁹ S. Rajagopalan and R. Robb. Schwarz meets Schwann: Design and fabrication of biomorphic and durataxic tissue engineering scaffolds. *Medical Image Analysis*, 10(5):693–712, October 2006.
- ¹⁰ Thomas Lenosky, Xavier Gonze, Michael Teter, and Vert Elser. Energetics of negatively curved graphitic carbon. *Nature*, 355(6358):333–335, January 1992.
- ¹¹ David Vanderbilt and J. Tersoff. Negative-curvature fullerene analog of C₆₀. *Phys. Rev. Lett.*, 68:511–513, Jan 1992.
- ¹² Katsuaki Kawasumi, Qianyan Zhang, Yasutomo Segawa, Lawrence T Scott, and Kenichiro Itami. A grossly warped nanographene and the consequences of multiple odd-membered-ring defects. *Nature Chemistry*, 5(9):739–744, September 2013.
- ¹³ E Barborini, P Piseri, P Milani, G Benedek, C Ducati, and J Robertson. Negatively curved spongy carbon. *Applied Physics Letters*, 81(18):3359–3361, 2002.
- ¹⁴ Khanin Nueangnoraj, Hiroto Nishihara, Katsuaki Imai, Hiroyuki Itoi, Takafumi Ishii, Manabu Kiguchi, Yohei Sato, Masami Terauchi, and Takashi Kyotani. Formation of crosslinked-fullerene-like framework as negative replica of zeolite Y. *Carbon*, 62(C):455–464, October 2013.
- ¹⁵ Yoshikazu Ito, Yoichi Tanabe, H J Qiu, Katsuaki Sugawara, Satoshi Heguri, Ngoc Han Tu, Khuong Kim Huynh, Takeshi Fujita, Takashi Takahashi, Katsumi Tanigaki, and Mingwei Chen. HighQuality ThreeDimensional Nanoporous Graphene. *Angewandte Chemie*, 126(19):4922–4926, March 2014.
- ¹⁶ Yoshikazu Ito, H J Qiu, Takeshi Fujita, Yoichi Tanabe, Katsumi Tanigaki, and Mingwei Chen. Bicontinuous Nanoporous Ndoped Graphene for the Oxygen Reduction Reaction. *Advanced Materials*, 26(24):4145–4150, April 2014.
- ¹⁷ Makoto Tagami, Yunye Liang, Hisashi Naito, Yoshiyuki Kawazoe, and Motoko Kotani. Negatively curved cubic carbon crystals with octahedral symmetry. *Carbon*, 76:266–274, September 2014.
- ¹⁸ <http://www.openmx-square.org>.
- ¹⁹ M Z Hasan and C L Kane. Colloquium: topological insulators. *Reviews of Modern Physics*, 82(4):3045, 2010.

- ²⁰ X L Qi and S C Zhang. Topological insulators and superconductors. *Reviews of Modern Physics*, 83(4):1057, 2011.
- ²¹ Liang Fu, C Kane, and E Mele. Topological Insulators in Three Dimensions. *Physical Review Letters*, 98(10):106803, March 2007.
- ²² A. A. Burkov, M. D. Hook, and Leon Balents. Topological nodal semimetals. *Phys. Rev. B*, 84:235126, Dec 2011.
- ²³ Zhijun Wang, Yan Sun, Xing-Qiu Chen, Cesare Franchini, Gang Xu, Hongming Weng, Xi Dai, and Zhong Fang. Dirac semimetal and topological phase transitions in $A_3\text{Bi}$ ($A=\text{Na}, \text{K}, \text{Rb}$). *Physical Review B*, 85(19):195320, May 2012.
- ²⁴ Zhijun Wang, Hongming Weng, Quansheng Wu, Xi Dai, and Zhong Fang. Three-dimensional dirac semimetal and quantum transport in Cd_3As_2 . *Physical Review B*, 88(12):125427, September 2013.
- ²⁵ Z. K. Liu, B. Zhou, Y. Zhang, Z. J. Wang, Hongming Weng, D. Prabhakaran, S.-K. Mo, Z. X. Shen, Z. Fang, X. Dai, Z. Hussain, and Y. L. Chen. Discovery of a three-dimensional topological dirac semimetal, Na_3Bi . *Science*, 343(6173):864–867, 2014.
- ²⁶ Z K Liu, J Jiang, B Zhou, Z J Wang, Y Zhang, H M Weng, D Prabhakaran, S K Mo, H Peng, P Dudin, T Kim, M Hoesch, Z Fang, X Dai, Z.-X. Shen, D. L. Feng, Z Hussain, and Y L Chen. A stable three-dimensional topological Dirac semimetal Cd_3As_2 . *Nature Materials*, 13:677–681, May 2014.
- ²⁷ Madhab Neupane, Su-Yang Xu, Raman Sankar, Nasser Alidoust, Guang Bian, Chang Liu, Ilya Belopolski, Tay-Rong Chang, Horng-Tay Jeng, Hsin Lin, Arun Bansil, Fangcheng Chou, and M Zahid Hasan. Observation of a three-dimensional topological Dirac semimetal phase in high-mobility Cd_3As_2 . *Nature Communications*, 5:3786, 2014.
- ²⁸ Sergey Borisenko, Quinn Gibson, Danil Evtushinsky, Volodymyr Zabolotnyy, Bernd Büchner, and Robert J. Cava. Experimental realization of a three-dimensional dirac semimetal. *Phys. Rev. Lett.*, 113:027603, Jul 2014.
- ²⁹ Yoshikazu Ito and Chen Mingwei. Private Communication.
- ³⁰ Xiangang Wan, Ari M. Turner, Ashvin Vishwanath, and Sergey Y. Savrasov. Topological semimetal and fermi-arc surface states in the electronic structure of pyrochlore iridates. *Phys. Rev. B*, 83:205101, May 2011.
- ³¹ Gang Xu, Hongming Weng, Zhijun Wang, Xi Dai, and Zhong Fang. Chern semimetal and the

- quantized anomalous hall effect in HgCr_2Se_4 . *Physical Review Letters*, 107(18):186806, October 2011.
- ³² Gábor B. Halász and Leon Balents. Time-reversal invariant realization of the weyl semimetal phase. *Phys. Rev. B*, 85:035103, Jan 2012.
- ³³ A. A. Burkov and Leon Balents. Weyl semimetal in a topological insulator multilayer. *Physical Review Letters*, 107(12):127205, September 2011.
- ³⁴ Shinsei Ryu and Yasuhiro Hatsugai. Topological Origin of Zero-Energy Edge States in Particle-Hole Symmetric Systems. *Physical Review Letters*, 89(7):077002, July 2002.
- ³⁵ T.T. Heikkilä and G.E. Volovik. Dimensional crossover in topological matter: Evolution of the multiple dirac point in the layered system to the flat band on the surface. *JETP Letters*, 93(2):59–65, 2011.
- ³⁶ T.T. Heikkilä, N.B. Kopnin, and G.E. Volovik. Flat bands in topological media. *JETP Letters*, 94(3):233–239, 2011.
- ³⁷ G. E. Volovik. Topology of quantum vacuum. *ArXiv:1111.4627*, November 2011.
- ³⁸ Hongming Weng, Xi Dai, and Zhong Fang. Exploration and prediction of topological electronic materials based on first-principles calculations. *MRS Bulletin*, 39:849–858, 10 2014.
- ³⁹ N. B. Kopnin, T. T. Heikkilä, and G. E. Volovik. High-temperature surface superconductivity in topological flat-band systems. *Phys. Rev. B*, 83:220503, Jun 2011.
- ⁴⁰ G. E. Volovik. From Standard Model of particle physics to room-temperature superconductivity. *ArXiv:1409.3944*, September 2014.
- ⁴¹ Roger S. K. Mong and Vasudha Shivamoggi. Edge states and the bulk-boundary correspondence in dirac hamiltonians. *Phys. Rev. B*, 83:125109, Mar 2011.
- ⁴² Ling Lu, Liang Fu, John D Joannopoulos, and Marin Soljačić. Weyl points and line nodes in gyroid photonic crystals. *Nature Photonics*, 7(4):294–299, March 2013.
- ⁴³ G P Mikitik and Yu V Sharlai. Band-contact lines in the electron energy spectrum of graphite. *Physical Review B*, 73(23):235112, June 2006.
- ⁴⁴ G P Mikitik and Yu V Sharlai. The Berry phase in graphene and graphite multilayers. *Low Temperature Physics*, 34(1):794–800, October 2008.
- ⁴⁵ K. Mullen, B. Uchoa, and D. T. Glatzhofer. Line of Dirac Nodes in Hyper-Honeycomb Lattices. *ArXiv:1408.5522*, August 2014.
- ⁴⁶ Aurélien Lherbier, Humberto Terrones, and Jean-Christophe Charlier. Three-dimensional mass-

less dirac fermions in carbon schwarzites. *Phys. Rev. B*, 90:125434, Sep 2014.

⁴⁷ Shengyuan A Yang, Hui Pan, and Fan Zhang. Dirac and Weyl Superconductors in Three Dimensions. *Physical Review Letters*, 113(4):046401, July 2014.

⁴⁸ Y. Chen, Y. Xie, S. A. Yang, H. Pan, F. Zhang, M. L. Cohen, and S. Zhang. Spin-orbit-free Weyl-loop and Weyl-point semimetals in a stable three-dimensional carbon allotrope. *ArXiv:1505.02284*, May 2015.

⁴⁹ J. C. Slater and G. F. Koster. Simplified lcao method for the periodic potential problem. *Phys. Rev.*, 94:1498–1524, Jun 1954.

Appendix A: Tight-binding Model

1. 6-1-1-p case

The hypothetic atomic orbital basis set is arranged in the order of $g_{xy(x^2-y^2)}$, $g_{yz(y^2-z^2)}$, $g_{zx(z^2-x^2)}$, $f_{x(y^2-z^2)}$, $f_{y(z^2-x^2)}$ and $f_{z(x^2-y^2)}$. Those from g (f) orbitals are triple-degenerate and the on-site energy is set as E_g (E_f). Since the cubic symmetry, only $g_{xy(x^2-y^2)}$ orbital is plotted in the xy plane in Figure S1. The $f_{x(y^2-z^2)}$ is plotted as two parts f_{xy^2} and $-f_{xz^2}$, perpendicular to each other. Arranging these orbitals on a simple cubic lattice with lattice constant a , the Slater-Koster parameters for nearest-neighbor hopping is defined in the following. The nearest hopping between $g_{xy(x^2-y^2)}$ in x and y direction is V_{gpp} , while that in z direction is V_{gpd} . The hopping between f_{xy^2} ($-f_{xz^2}$) along x and y (x and z) is V_{ffp} , and that along z (y) direction is V_{ffd} . The hopping between nearest neighboring $g_{xy(x^2-y^2)}$ and f_{xy^2} ($-f_{xz^2}$) along y direction is V_{fgp} (V_{fgd}), while those along x and z direction are zero. We list some of the nonzero elements of final tight-binding hamiltonian and others can be easily derived by using the cubic cyclic symmetry.

$$\begin{aligned} H_{g_{xy(x^2-y^2)}, g_{xy(x^2-y^2)}} &= E_g + 2 \cos(\vec{k} \cdot \vec{a}_x) V_{gpp} \\ &\quad + 2 \cos(\vec{k} \cdot \vec{a}_y) V_{gpp} + 2 \cos(\vec{k} \cdot \vec{a}_z) V_{gpd} \end{aligned}$$

$$\begin{aligned} H_{g_{xy(x^2-y^2)}, f_{x(y^2-z^2)}} &= i * 2 \sin(\vec{k} \cdot \vec{a}_y) V_{fgp} \\ &\quad + i * 2 \sin(\vec{k} \cdot \vec{a}_y) V_{fgd} \end{aligned}$$

$$H_{g_{xy(x^2-y^2)}, f_{y(z^2-x^2)}} = i * 2 \sin(\vec{k} \cdot \vec{a}_x) V_{fgp}$$

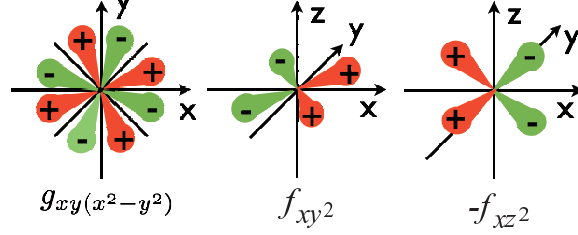


Figure S1. The angular distribution of $g_{xy(x^2-y^2)}$, f_{xy^2} and $-f_{xz^2}$ orbitals.

$$+i * 2 \sin(\vec{k} \cdot \vec{a}_x) V_{fgd}$$

$$\begin{aligned}
H_{f_{x(y^2-z^2)}, f_{x(y^2-z^2)}} &= E_f \\
+2 \cos(\vec{k} \cdot \vec{a}_x) V_{ffp} &+ 2 \cos(\vec{k} \cdot \vec{a}_x) V_{ffp} \\
-2 \cos(\vec{k} \cdot \vec{a}_y) V_{ffp} &- 2 \cos(\vec{k} \cdot \vec{a}_y) V_{ffd} \\
-2 \cos(\vec{k} \cdot \vec{a}_z) V_{ffp} &- 2 \cos(\vec{k} \cdot \vec{a}_z) V_{ffd}
\end{aligned}$$

Here \vec{a}_x , \vec{a}_y and \vec{a}_z are the nearest neighbor site along positive x , y and z direction, respectively. We have fitted all the Slater-Koster parameters and find that $E_g=-0.12$, $E_f=0.19$, $V_{ffp}=0.019$, $V_{ffd}=-0.075$, $V_{fgp}=0.05$, $V_{fgd}=0.0$, $V_{ggp}=-0.035$, $V_{ggd}=-0.055$ (all in unit eV) can well reproduce the band structure from first-principles calculation as shown in Fig. 2 of main text.

However, the following set of parameters will modify the band structure by shifting the band crossing from R-M to Γ -M. The band structure with $E_g=-0.10$, $E_f=0.16$, $V_{ffp}=-0.010$, $V_{ffd}=-0.080$, $V_{fgp}=0.05$, $V_{fgd}=0.0$, $V_{ggp}=-0.055$, $V_{ggd}=-0.035$ is shown in Figure S2. Compared with that in realistic case, there is additional band inversion at M. This changes the Z_2 index to be (0;111) if the tiny SOC is considered.

2. 6-1-2-p case

For 6-1-2-p case, the band structure from first-principles calculation is shown in Figure S3. Obviously, there are band inversion around M point. Careful analysis has shown that the occupied and unoccupied triply degenerated bands at Γ (also at R point) are T_{1u} and T_{2g} , respectively. Therefore, we can take hypothetic p_x , p_y and p_z orbitals as the basis for T_{1u} representation in cubic symmetry and d_{xy} , d_{yz} and d_{zx} form T_{2g} . All the p orbitals have on-site energy E_p and d orbitals have E_d . The Slater-Koster parameters such as $V_{pp\sigma}$, $V_{pp\pi}$,

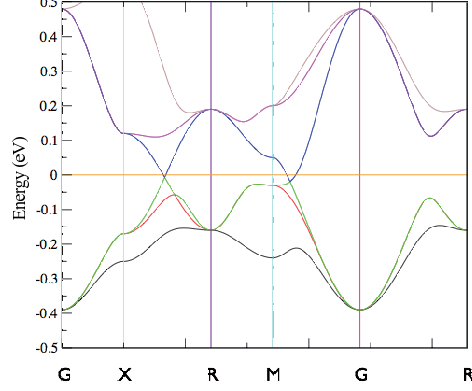


Figure S2. The tight-binding band structure with $E_g=-0.10$, $E_f=0.16$, $V_{ffp}=-0.010$, $V_{ffd}=-0.080$, $V_{fgp}=0.05$, $V_{fgd}=0.0$, $V_{ggp}=-0.055$, $V_{ggd}=-0.035$. The band crossing point is shifted from R-M to M- Γ compared with Fig. 3 in main text.

$V_{dd\pi}$, $V_{dd\delta}$ and $V_{pd\pi}$ are defined as in common.⁴⁹ Putting these orbitals on a simple cubic lattice, we can have the tight-binding Hamiltonian and some of the nonzero elements are listed as following:

$$H_{x,x} = E_p + 2 \cos(\vec{k} \cdot \vec{a}_x) V_{pp\sigma} + 2 \cos(\vec{k} \cdot \vec{a}_y) V_{pp\pi} + 2 \cos(\vec{k} \cdot \vec{a}_z) V_{pp\pi}$$

$$H_{x,xy} = i * 2 \sin(\vec{k} \cdot \vec{a}_y) V_{pd\pi}$$

$$H_{x,zx} = i * 2 \sin(\vec{k} \cdot \vec{a}_z) V_{pd\pi}$$

$$H_{xy,xy} = E_d + 2 \cos(\vec{k} \cdot \vec{a}_x) V_{dd\pi} + 2 \cos(\vec{k} \cdot \vec{a}_y) V_{dd\pi} + 2 \cos(\vec{k} \cdot \vec{a}_z) V_{dd\delta}$$

The other elements can be obtained by using cubic cyclic symmetry. The fitted parameters which can well reproduce the band structure from first-principles calculation are $E_p=-0.10147$, $E_d=0.28281$, $V_{pp\sigma}=0.02005$, $V_{pp\pi}=-0.017848$, $V_{pd\pi}=0.034711$, $V_{dd\pi}=0.04694$, $V_{dd\delta}=-0.062523$. The mean square error, around 0.0061 eV^2 , is estimated for the three conduction bands. Estimation for the valence bands has problem in selecting proper bands since there are more than three bands entangled. While the topology of bands from fitted model is the same as from first-principles calculation.

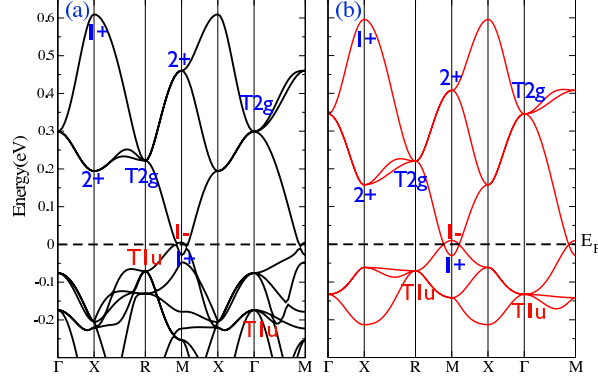


Figure S3. The band structure of 6-1-2-p case calculated from (a) first-principles and (b) tight-binding model, respectively. The symmetrical representation, degeneracy and parity of relevant bands are labeled.

Appendix B: Real Valued Hamiltonian for Spinless System with Both Time-reversal and Inversion Symmetry

We will show that for a spinless system with both time-reversal (T) and inversion (P) symmetry its Bloch Hamiltonian $H(\mathbf{k})$ can always be taken as real valued under some certain gauge choice. To be general, plane waves $e^{i(\mathbf{k}+\mathbf{G}_n)\cdot\mathbf{r}}$ are taken as basis set to describe $H(\mathbf{k})$, where \mathbf{G}_n are the reciprocal lattice vectors. With the above chosen basis set, the invariance under time reversal operator T can be expressed as,

$$\hat{T}H(\mathbf{k})\hat{T}^{-1} = \hat{O}H^*(\mathbf{k})\hat{O}^{-1} = H(-\mathbf{k})$$

and that of the inversion symmetry reads

$$\hat{O}H(\mathbf{k})\hat{O}^{-1} = H(-\mathbf{k})$$

, where the unitary matrix \hat{O} can be defined as $\hat{O}_{nm} = 1$ for $n = -m$ and zero for all the other matrix elements. From the above two equations, it is obvious that $H(\mathbf{k})$ is real.

Appendix C: Topology of bulk Node-line Hamiltonian

As shown in main text, the effective hamiltonian for bulk Node-line state can be written as

$$H(k_x, k_y, k_z) = \mathbf{d}(k_x, k_y, k_z) \cdot \boldsymbol{\sigma}$$

, where $\mathbf{d}=(d_x, d_y, d_z)$ and $\sigma = (\sigma_x, \sigma_y, \sigma_z)$. Taking $d_x=k_z$, $d_y=0$ and $d_z=M - B(k_x^2 + k_y^2 + k_z^2)$ can reproduce the bulk node-line state when $\frac{M}{B} > 0$. According to R. S. K. Mong et al.⁴¹, to check its boundary state in surface perpendicular to k_z this bulk hamiltonian should be reformulated as

$$\begin{aligned} H(k_{\parallel}, k_z) &= \mathbf{c}_0 + \mathbf{c}_1 k_z + \mathbf{c}_2 k_z^2 \\ &= (0, 0, M - Bk_{\parallel}^2) + (1, 0, 0)k_z + (0, 0, -B)k_z^2. \end{aligned}$$

Here k_{\parallel} denotes in-plane coordinates (k_x, k_y) and \mathbf{c}_0 , \mathbf{c}_1 and \mathbf{c}_2 are vectors in space spanned by σ . The above bulk hamiltonian is parabola in plane spanned by \mathbf{c}_1 and \mathbf{c}_2 . Its origin is within the concave side of the parabola when $k_{\parallel}(k_x, k_y)$ taking the value satisfying $k_x^2 + k_y^2 < \frac{M}{B}$. Thus, there is topologically protected surface states nestled inside of projected node-line with zero eigen energy to form “drumhead”-like state.